

## Development of an X-ray pixel detector with multi-port charge-coupled device for X-ray free-electron laser experiments

Takashi Kameshima, Shun Ono, Togo Kudo, Kyosuke Ozaki, Yoichi Kirihaara, Kazuo Kobayashi, Yuichi Inubushi, Makina Yabashi, Toshio Horigome, Andrew Holland, Karen Holland, David Burt, Hajime Murao, and Takaki Hatsui

Citation: [Review of Scientific Instruments](#) **85**, 033110 (2014); doi: 10.1063/1.4867668

View online: <http://dx.doi.org/10.1063/1.4867668>

View Table of Contents: <http://scitation.aip.org/content/aip/journal/rsi/85/3?ver=pdfcov>

Published by the [AIP Publishing](#)

---

An advertisement for Extrel Core Mass Spectrometers. The background is a photograph of a man and a woman in white lab coats working with molecular models. On the left, text reads 'Discover the IQ-2000— A new way to INSPIRE.' Below this, a grey box contains the text 'Visit us at Pittcon and ACS.' On the right, the Extrel logo is displayed, featuring a stylized 'E' made of colorful dots and the text 'Extrel Core Mass Spectrometers'.

# Development of an X-ray pixel detector with multi-port charge-coupled device for X-ray free-electron laser experiments

Takashi Kameshima,<sup>1,a)</sup> Shun Ono,<sup>2,a)</sup> Togo Kudo,<sup>2</sup> Kyosuke Ozaki,<sup>2</sup> Yoichi Kirihiro,<sup>2</sup> Kazuo Kobayashi,<sup>2</sup> Yuichi Inubushi,<sup>2</sup> Makina Yabashi,<sup>1,2</sup> Toshio Horigome,<sup>3</sup> Andrew Holland,<sup>4</sup> Karen Holland,<sup>4</sup> David Burt,<sup>5</sup> Hajime Murao,<sup>6</sup> and Takaki Hatsui<sup>1,2,b)</sup>

<sup>1</sup>JASRI, 1-1-1 Kouto, Sayo-cho, Sayo-gun, Hyogo 679-5198, Japan

<sup>2</sup>RIKEN SPring-8 Center, 1-1-1 Kouto, Sayo-cho, Sayo-gun, Hyogo 679-5148, Japan

<sup>3</sup>Institute for Molecular Science, Myodaiji, Okazaki 444-8585, Japan

<sup>4</sup>XCam, Ltd, 2 Stone Circle Road, Round Spinney Industrial Estate, Northampton NN3 8RF, United Kingdom

<sup>5</sup>e2v, 106 Waterhouse Lane, Chelmsford, Essex CM1 2QU, United Kingdom

<sup>6</sup>Meisei Electric Co. Ltd, Naganuma 2223, Isesaki, Gunma 372-8585, Japan

(Received 1 November 2013; accepted 23 February 2014; published online 26 March 2014)

This paper presents development of an X-ray pixel detector with a multi-port charge-coupled device (MPCCD) for X-ray Free-Electron laser experiments. The fabrication process of the CCD was selected based on the X-ray radiation hardness against the estimated annual dose of  $1.6 \times 10^{14}$  photon/mm<sup>2</sup>. The sensor device was optimized by maximizing the full well capacity as high as 5 Me- within 50  $\mu$ m square pixels while keeping the single photon detection capability for X-ray photons higher than 6 keV and a readout speed of 60 frames/s. The system development also included a detector system for the MPCCD sensor. This paper summarizes the performance, calibration methods, and operation status. © 2014 Author(s). All article content, except where otherwise noted, is licensed under a Creative Commons Attribution 3.0 Unported License. [<http://dx.doi.org/10.1063/1.4867668>]

## I. INTRODUCTION

Recent advances in X-ray Free-Electron Laser (XFEL) technologies have enabled the production of full spatial coherence, ultra-short pulse duration, and high brilliance lasers in the X-ray frequency domain.<sup>1,2</sup> These novel light source characteristics promise development of a wide range of applications, with some already demonstrating new capabilities. From an experimental point of view, the XFEL pulse characteristics fluctuate shot-by-shot due to inherent characteristics of the Self-Amplified Spontaneous Emission amplification scheme or other possible instabilities in the linear accelerator. The high intensity of XFEL pulses can cause irreversible sample damage with single-shot irradiation. Therefore, samples are exchanged or scanned in many experiments in order to avoid the effects of X-ray damage. Measurements must be synchronized to the XFEL pulse in order to analyze the data correlation between XFEL pulse characteristics and/or the sample identity. To meet these demands, various X-ray pixel detector development programs have been carried out or are currently in progress.<sup>3-7</sup> One of the main goals is enabling single-photon-detection while maximizing the detectable peak signal.

This paper presents the development of a multi-port charge-coupled device (MPCCD) detector that is optimized for experiments at the SACLA facility.<sup>2</sup> The detector and its concept, however, have versatile applicability to general XFEL experiments. The goal is to develop a detector family

for a wide range of scientific applications. Considering typical requirements which cannot be achieved by commercially-off-the-shelf (COTS) detectors, we established the essential performance requirements as (1) a single X-ray photon sensitivity for the 6-12 keV range, (2) a frame rate of 60 Hz matching to the pulse rate of SACLA, (3) a tiled detector with a dead width of no more than 6 pixels between the tiles, and (4) X-ray radiation hardness over 1 annual dose. Under these constraints, we were able to maximize the peak signal to 4.1–5.0 Me- with 50  $\mu$ m square pixels.

One of the detector technologies capable of single X-ray photon detection is direct-detection CCDs, which are widely used, especially in X-ray astronomy. Successful examples can be found in several X-ray observatories such as Yohkoh,<sup>8</sup> ASCA,<sup>9,10</sup> Chandra,<sup>11</sup> Newton,<sup>12,13</sup> and Suzaku.<sup>14</sup> These observatories are designed to record signal intensity as low as a single X-ray photon due to the sparse signal rate. Therefore these X-ray astronomy technologies are not directly transferrable to XFEL applications. A faster readout rate of 60 frame/s, X-ray radiation hardness, and a higher peak signal should especially be investigated and incorporated into future development.

This paper describes the development of MPCCD detectors. This paper is organized as follows:

- Section II presents the optimization of sensor design to meet SACLA requirements including the selection of the CCD fabrication process, and design trade-offs.
- Section III provides an overview of the detector system.
- Section IV combines the evaluation results of the performance, calibration, and deployment status.
- Finally, Sec. V presents the conclusions and outlook.

<sup>a)</sup>T. Kameshima and S. Ono contributed equally to this work.

<sup>b)</sup>T. Hatsui initiated and directed the study, and wrote the paper. Author to whom correspondence should be addressed. Electronic mail: hatsui@spring8.or.jp



## II. MULTI-PORT CCD SENSOR

### A. Fabrication process

CCDs are widely used for scientific imaging, automated inspection, and consumer applications. In X-ray applications, two types of detector configurations are common, namely, indirect detection and direct detection. The former is generally composed of a phosphor, where X-rays are converted to optical photons, and a fiber-optics plate.<sup>15</sup> The amount of signal charge generated by a single X-ray photon within the CCD device,  $N_{\text{sig}}$ , is generally less than 200 electron-hole pairs due to the inherent small charge generation with large effective ionization energy and due to the lower transmission efficiency from the phosphor to the CCD sensor. On the contrary, each X-ray photon in the direct detection scheme produces more than 1000 electron-hole pairs.<sup>16</sup> The signal charge,  $N_c$ , is expressed by  $N_c = E_{ph}/W$ , where  $W$  is the average energy required to create an electron-hole pair. In addition, the X-ray to charge conversion in silicon through the dominant photoelectric process has a small conversion gain variation,  $\sigma_s = \sqrt{F \cdot N_c}$  [e-], due to the correlated conversion process, which is quantitatively expressed by the small Fano factor,  $F$ . The lowest target photon energy of the present sensor is 6 keV, which determines the noise specification of the sensor. In the case of a 5.9 keV photon,  $W$  is reported to be 3.658 eV, which is slightly higher than the asymptotic value of 3.65 eV for a higher photon energy, and  $F$  is 0.12.<sup>17,18</sup> The single 5.9 keV photon generates about 1600 e-h pairs with a standard deviation of about 14 e- rms.<sup>19</sup> The larger signal charge from a single photon in addition to the small conversion gain variance significantly reduces the required readout noise, and makes the direct detection scheme advantageous for single photon detection, especially for higher frame rates. In fact, several development programs for XFEL imaging detectors have adopted the direct detection scheme.<sup>3-7</sup> In the work we present in this paper, we also chose to use a direct-detection configuration. In addition, we used a metal-oxide insulator (MOS) CCD structure, which is the standard CCD process in industry in order to guarantee prompt and stable production.

The drawback of the direct detection MOS CCD is weaker radiation hardness. In contrast to the indirect configuration, where fiber-optic plates absorb X-rays and protect the sensor, the direct detection configuration requires the sensor to be illuminated by X-rays. Here we presume the annual fluence to be  $1.6 \times 10^{14}$  photons/mm<sup>2</sup> at 12 keV, which is equiv-

alent to an average signal of 500 photons/pixel with 50  $\mu\text{m}$  square pixels and operation at a rate of 60 frames/s for 150 days per year. Thin silicon illuminated by this annual fluence corresponds to 0.58 MGy(Si) if we assume the charged-particle equilibrium (CPE) condition. Note that the CPE is not well satisfied due to the large dose gradient and detailed simulations are required to assess the dose. The radiation tolerance for MOS CCDs against such a high X-ray dose has not yet been investigated.

The X-ray-matter interaction in silicon when photon energy is less than 60 keV is dominated by the photoelectric effect.<sup>20</sup> Thus X-ray radiation damage arises from the total ionizing dose. The non-ionizing dose effect that causes displacement of atoms is negligible. The photoelectric effect induces X-rays absorbed in silicon to generate electron-hole pairs, which are swept by the local electric field. X-rays absorbed in silicon oxides result in the production of electron-hole pairs, where only electrons move out of the oxides. The holes are generally trapped at the silicon-oxide interface.<sup>21</sup> The MOS CCD structure has an oxide layer between the gate electrodes and the silicon. The trapped holes generally cause additional dark current and shift the flat-band voltage to degrade the charge-transfer efficiency (CTE) (these conditions can ultimately upset the voltage balance of the output amplifier leading to the device ceasing to operate). The quantitative prediction of the X-ray radiation effect is generally not straightforward in actual device structures.

In order to assess the radiation hardness of the MOS CCD, experimental evaluation has been carried out for commercially available CCD structures, namely, a front-illuminated standard gate structure (device type A), front-illuminated device with a radiation hard gate structure (device type B), and back-illuminated device with a standard gate structure onto bulk silicon (device type C). Some of the structure parameters are described in Table I. All these devices are made by e2v, Ltd. The radiation hard gate structure has thinner silicon oxide than the standard gate structure.

The irradiation was carried out at the beamline BL29XU of SPring-8.<sup>22</sup> Before and after the X-ray irradiation, the dark current was measured while the devices were driven at a temperature around  $-40^\circ\text{C}$ . The effect of X-ray radiation is known to be sensitive to the internal electric field across the oxide during the radiation. A stronger electric field generally enhances the radiation degradation because of the decrease of the electron-hole recombination rate at the initial radiation

TABLE I. Device structure and dark current after X-ray radiation.

Device	Device type	Illumination side	Gate dielectric	Sensor silicon thickness ( $\mu\text{m}$ )	$D_{\text{FM}}$ ( $\mu\text{A}/\text{cm}^2$ ) after X-ray radiation <sup>a</sup>			$T^{\text{b}}(^{\circ}\text{C})$
					$\times 0.1^{\text{c}}$	$\times 0.3^{\text{c}}$	$\times 1.0^{\text{c}}$	
A	CCD47-20	Front	Standard <sup>d</sup>	50	0.65	1.6	2.2	-35
B	CCD47-20	Front	Rad. hard <sup>d</sup>	50	0.28	0.85	1.1	-30
C	CCD30-11	Back	Standard <sup>e</sup>	70	0.33	0.85	2.0	-34
MPCCD	CCD262-50	Front	Rad. hard <sup>d</sup>	50	0.04	0.11	0.25	-17

<sup>a</sup>Dark current projected to performance at 300 K.

<sup>b</sup>Temperature required for acceptable performance after a presumed annual dose.

<sup>c</sup>Annual X-ray fluence is presumed to be  $1.6 \times 10^{14}$  photons/mm<sup>2</sup>. See text for details.

<sup>d</sup>Gate structure is fabricated onto epitaxial silicon with a non-inverted mode.

<sup>e</sup>Gate structure is fabricated onto bulk silicon with a non-inverted mode.

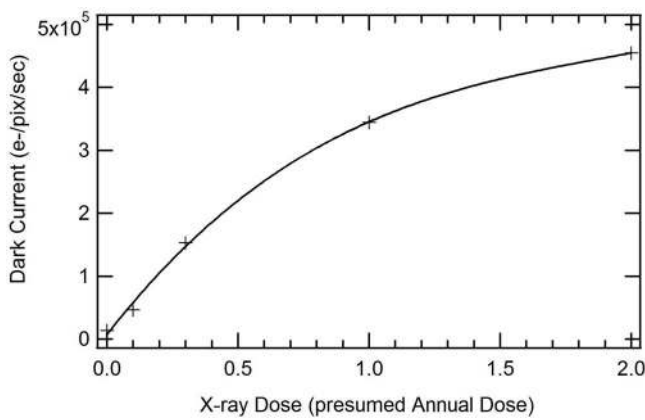


FIG. 1. The measured dark current before and after X-ray dose of 0.1, 0.33, 1.0, and 2.0 annual doses recorded at  $-30^{\circ}\text{C}$  (+). Annual X-ray fluence is presumed to be  $1.6 \times 10^{14}$  photons/ $\text{mm}^2$  at the photon energy of 12 keV. An eye-friendly line obtained by a fitting to fourth-order polynomial is shown as well.

process,<sup>21</sup> in which a few thousand electron-hole pairs are generated in a microscopic space after X-ray photon absorption. In the experiment, X-ray illumination was carried out with voltages under the exposure operation condition, i.e., two out of three image gates were connected to +10 V to mimic conditions during XFEL data recording. The CCD drain implants were biased high, at  $\sim 20$  V to remove the generated charge. The X-ray beam was shaped into a rectangle by using a slit. The exposed region of the sensor was moved during the exposure to create trapezoidal illumination spots along the column direction in order to remove sharp boundaries at the pixel level from the irradiation exposure spots. The slope boundary had a slope of one annual dose per 1 mm. This implies that it is steep enough to represent most of XFEL applications. A significant increase of the dark current was observed after the X-ray dose as shown in Fig. 1. The increase of the dark current was partly saturated after two presumed annual dose. This can be explained by the saturation of the intermediate state density produced by the X-ray dose. In order to confirm the reproducibility, more than two devices were tested for each device type. Lot difference gave  $\pm 10\%$  maximum difference in dark current figure of merit ( $D_{FM}$ ) after one annual dose, which is defined below.

The temperature dependence of the dark current was also measured. The results indicate that the temperature dependence of the dark current for both pre- and post-irradiation cases is accurately expressed within standard error by the following equation for surface and depletion dark current:<sup>16</sup>

$$D_R(e^-) = 2.5 \times 10^{15} P_s D_{FM} T^{1.5} e^{-E_g/(2kT)}, \quad (1)$$

where  $P_s$  is the pixel area ( $\text{cm}^2$ ),  $D_{FM}$  is the dark current figure of merit defined as dark current at 300 K ( $\text{nA}/\text{cm}^2$ ),  $T$  is the temperature (K),  $k$  is the Boltzmann constant, and  $E_g$  is the bandgap energy (eV) of silicon.

The measured dark current figure of merit,  $D_{FM}$ , for these devices is provided in Table I. Nominal annual fluences of 0.1, 0.3, and 1.0 at 12 keV were dosed onto the sensors. As discussed later in Sec. II C, the noise induced by the dark current was specified to be less than 100 e- rms/pixel/frame with

50  $\mu\text{m}$  pixels. This corresponds to 10 000 e-/pixel/frame. In a full-frame-transfer architecture, the signal is transferred by imaging pixels, and therefore the measurable dark charge is accumulated during the exposure and the readout time. For the SACLA facility with a 60 Hz repetition rate design, the accumulation time should be less than the shot interval and the dark current therefore should be less than 600 000 e-/pixel/s. Lowering the device temperature can reduce the dark current. The operation temperature that is required to meet the dark current specifications after one annual dose is also summarized in Table I. These results indicate that any of these device structures will meet the requirement if the device is cooled down to  $-35^{\circ}\text{C}$ .

X-ray radiation also induces degradation of the charge transfer efficiency (CTE). The X-ray dose shifts the flat-band voltage by leaving a positive trapped hole inside the silicon dioxide layer beneath the CCD gates. The shift is dependent on the dose level. In other words, inhomogeneous dose may degrade the CTE irrespective of the dose amount by preventing transfer from one phase to the next. The CTE levels were measured for these devices as well. These devices indicated that CTE degradation sufficient to harm X-ray single photon sensitivity does not occur at least at the dose gradient of one presumed annual dose per 1 mm (the dose difference of  $1.6 \times 10^{14}$  photons/ $\text{mm}^2$  at 12 keV along 1 mm length). Device type B was selected since it performed best from the viewpoint of the dark current results.

## B. Point spread function and single photon detection

In the case of CCD and other pixel detector where the pixels are connected to a shared sensitive layer, the signal charge from single photon is often shared by multiple pixels. This phenomenon, called *charge sharing*, is important for defining the sensor specifications, especially the noise specification.<sup>23</sup>

In XFEL applications, detectors record pulsed X-ray photons within a few to tens of femto-seconds. The resulting transient signal charge inside the sensitive layer may provide a signal charge density higher than the doping concentration, which is called the high injection condition.<sup>24</sup> The internal potential collapses after the signal charge formation, and the charge collection is strongly coupled with the dynamics of the signal charge itself. The point-spread function (PSF) then depends on the signal intensity and signal time structure. Such non-local behavior is very difficult to calibrate practically and therefore should be carefully suppressed in the device design step.

In order to address both the charge sharing and the high injection effects, time dependent 3D device simulations were carried out using simulation code ATLAS3D ver. 5.17.11.C of Silvaco Inc. The mobility model, which includes the screening effect, electron-hole scattering, and carrier-carrier scattering, was used to describe charge dynamics under high injection.<sup>25</sup> The doping profile measured for the epitaxial silicon of the device type B was used. The temperature was set to 300 K, the highest temperature for operation. Under the bias voltage of 10.5 V, depletion depth of 40  $\mu\text{m}$  was obtained.



In order to simplify the analysis of the simulation and to determine the main physical process in the charge dynamics, a metal-silicon structure with an artificial work function was used to model the metal-insulator-silicon structure of the CCD. In this simplified model, all of the signal carriers sank to the metal and the charge collection step toward the buried channel could be described. The charge spilling within the buried channel after the charge collection was not considered within this model. It was considered to be independent from the charge injection condition and was taken into account in the pixel design step.

The signal charge generated by an X-ray photon was assumed to have a spherical shape with a diameter of  $1\ \mu\text{m}$  and a charge of  $3\ \text{ke}^-$ , which corresponds to a photon energy of  $11\ \text{keV}$ . The upper panel of Fig. 2 shows the simulated PSFs. All of the PSFs can be fitted well by a two dimensional Gaussian function. The standard deviation varies from  $1.7$ ,  $3.2$ ,  $3.8$ ,  $4.3$ , to  $5.6\ \mu\text{m}$  at injection depths of  $10$ ,  $30$ ,  $40$ ,  $45$ , and  $50\ \mu\text{m}$ , respectively. The PSF becomes broader with a deeper injection point. The relationship of the single photon detection capability, the readout noise, and the PSF is summarized in Appendix A. At a depth of  $50\ \mu\text{m}$ , the injection point is in the field-free region and lies immediately above the highly doped silicon, thus yielding the widest PSF. Under this worst

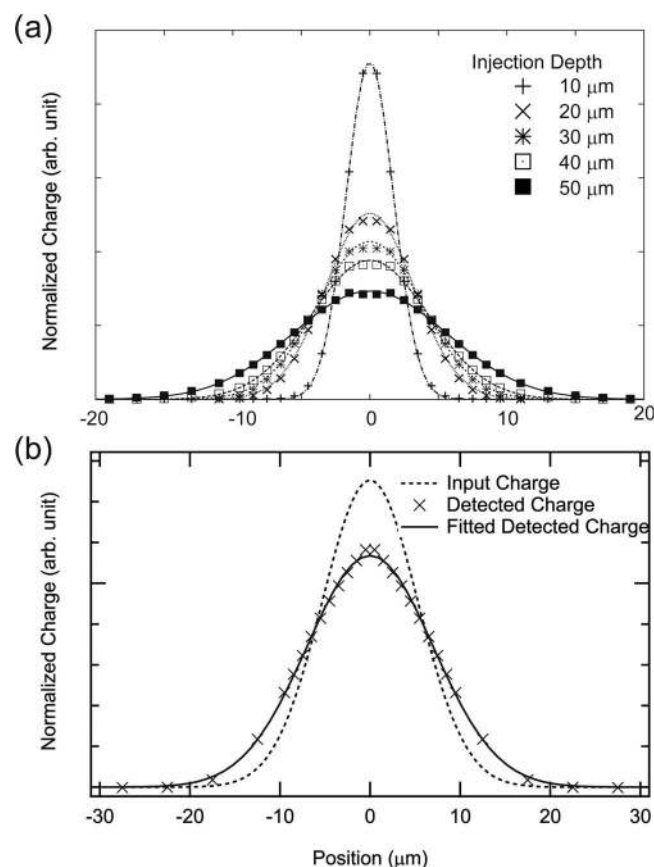


FIG. 2. Simulated PSF at a charge injection of  $3\ \text{ke}^-$  at several depth conditions from the metal-semiconductor surface (a). Injection depth at  $10$ ,  $20$ ,  $30$ ,  $40$ , and  $50\ \mu\text{m}$  resulted in PSF with a standard deviation of  $1.7$ ,  $3.2$ ,  $4.3$ , and  $5.6\ \mu\text{m}$ , respectively. The lower panel shows a  $5\ \text{Me}^-$  charge injection with a 2D Gaussian shape. The injection shape and simulated sensor response have standard deviations of  $5.3$  and  $7.0\ \mu\text{m}$ , respectively. These give a PSF with a standard deviation of  $4.6\ \mu\text{m}$  (b).

condition from the viewpoint of single photon detection, the un-detection probability defined in Appendix A is less than  $0.1$  if we achieve  $300\ \text{e}^-$  rms noise. Therefore we set the total noise performance goal to  $300\ \text{e}^-$  rms.

For the simulation under a high injection condition, a two-dimensional charge injection was assumed to have a Gaussian shape with a standard deviation of  $5.3\ \mu\text{m}$ . The resulting collected charge becomes blurred with a standard deviation of  $7.0\ \mu\text{m}$ . The corresponding PSF has a standard deviation of  $4.6\ \mu\text{m}$ . These results support a prediction that at least the selected process type B with  $50\ \mu\text{m}$  epitaxial silicon does not degrade the PSF up to a  $5\ \text{Me}^-$  signal injection, which is the target signal charge of the MPCCD sensor as discussed in Sec. II C. The present simulations indicate that even with the additional blur caused by high injection, the internal potential retains the ability to collect sufficient signal charge to maintain the PSF.

### C. Sensor design

Based on the discussion in Secs. II A and II B, we chose the fabrication process of the device type B (Table I). The device has a front-illumination structure. It is made from an epitaxial wafer with a p-type epitaxial layer with a thickness of  $50\ \mu\text{m}$  on top of a p-type low-resistivity wafer with a thickness of about  $600\ \mu\text{m}$ . The voltage applied to the gate structure on-top of the epitaxial layer depletes the epitaxial layer. The depletion depth reaches  $40\ \mu\text{m}$  according to the device simulation results based on the doping profile (Sec. II B). The rest of the epitaxial layer remains un-depleted (field-free region). The weak field causes degradation in the point-spread function (Sec. II B), but not in the quantum efficiency because the signal electron has long lifetime enough to be transferred to the depletion region without loss of the signal electron. Thus the epitaxial layer with a thickness of  $50\ \mu\text{m}$  forms the sensitive volume. The signal charge generated within the low-resistivity wafer will be quickly recombined and will not be detected by the sensor.

The sensor was then designed to optimize the full well, while achieving a readout noise of  $200\ \text{e}^-$  rms for single photon detection, a 3-side butttable design with dead width less than 6 pixels with an additional 4-side butttable option with stepped geometry, and a readout speed of 60 frames/s. Minimization of the heat dissipation on the sensor was also considered.

Fig. 3 shows the finalized schematic layout of the MPCCD sensor. Injection diodes were placed on top of the image pixel area to enable electronic measurement of the settling time, cross-talk, and flat-band voltage. The gate and drain tracks of the injection diodes (IG, ID) were connected to the wire-bonding pads through the metal tracks located on both sides of the imaging area. Alongside these tracks, metal tracks connected to the image pixel gates were placed. The space for these tracks can be an inactive (dead) area when the sensors are tiled. In order to minimize the dead width, two-phase pixels were chosen since this configuration requires the minimum number of tracks. The bandwidth of the image pixel gate tracks is determined mainly by the resistivity and

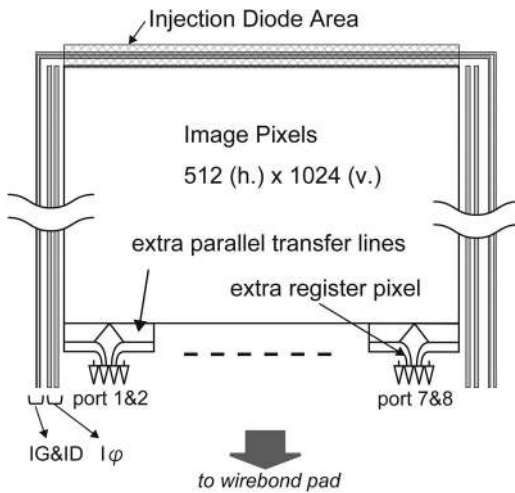


FIG. 3. The schematic layout of the MPCCD sensor. For both sides, there are two tracks connected to the gate and the drain of the injection diodes (IG and ID), and two tracks for the image pixel gates. The injection diode area is implemented on top of the imaging area. Six additional parallel transfer lines are placed to maintain the space for the bending region of the serial register, where four extra pixels exist in each amplifier port.

capacitance of the image gate tracks. We implemented the metal tracks with two metal layers to reduce resistivity. Note that we did not choose metal-buttressed image gates. The final optimized layout yielded a top and a side dead region with widths of  $150\ \mu\text{m}$  and  $300\ \mu\text{m}$ , respectively.

The pixel size was chosen to be  $50\ \mu\text{m}$ , significantly larger than COTS devices in order to increase the full well capacity of the imaging pixel. The CCD imaging pixel loses the stored charge by any of the following 3 pathways: (1) the stored charge touches the surface, resulting in poor CTE, (2) the spilling of the stored charge toward a neighboring column through the channel stop, or (3) vertical charge spilling toward a neighboring phase as the charge storage potential exceeds the barrier potential. Pathway 1 depends on the process type and the barrier potential used. The storage limit of the charge can be characterized by the capacitive charge storage in the unit storage area,  $N_s$ . The current process for a two-phase pixel has  $N_s = 7\text{--}8\ \text{ke}/\mu\text{m}^2$ . Both pathway 2 and pathway 3 demand a finite layout space almost independent of the pixel size. The full well capacity of an imaging pixel in this design scheme can be approximated by

$$Q_{FW} \sim N_s \frac{(N_p - 1)}{N_p} (L_h - G_h)(L_v - G_v), \quad (2)$$

where  $L_h$  and  $L_v$  are horizontal and vertical pixel lengths in  $\mu\text{m}$  unit, respectively.  $N_p$  is the number of the image gate phase.  $G_h$  and  $G_v$  are the gap spacing required to prevent pathways 2 and 3, respectively. In the selected two-phase image pixel ( $N_p = 2$ ),  $G_h$  and  $G_v$  are approximately  $5.5$  and  $6.5\ \mu\text{m}$ . For  $L_h = L_v = 50\ \mu\text{m}$ , we get an estimation of  $Q_{FW} = 5.7\text{--}6.6\ \text{Me-}$ . We did not implement the vertical overflow drain for anti-blooming because it results in a decrease of the pixel full well through the additional layout space and decreased  $N_s$ .<sup>26</sup> We should also note that for XFEL applications, a two-phase pixel configuration is superior to a three- or four-phase pixel schema because it simplifies the image

clock design. The two-phase pixel has a doped potential barrier along its row, which maintains the barrier shape even at the high injection condition. When using a three-, or four-phase pixel, where the barrier potential is made through the gate voltage,<sup>16</sup> the signal charge motion induces a transient mirror current onto the image gate line; a charge collection time of  $10\ \text{ns}$  for  $5\ \text{Me-}$  signal can result in a mirror current as high as  $80\ \mu\text{A}/\text{pixel}$ . Therefore, additional care should be taken in the image gate design.

To readout the full well capacity of  $5\ \text{Me-}$ , we need to transfer the charge to the on-chip amplifier without degrading the charge. Vertical analog binning will increase the signal charge, and hence the full wells of the serial registers are generally designed to be large enough to accommodate the cumulative charge. In this application, readout noise as discussed below is designed to be small enough for single photon detection. As a consequence, the binned mode is not mandatory for most applications except for a very small signal count rate, where the cumulative charge by binning can be assumed to be smaller than the pixel full well. Therefore the full well capacity of the serial register was chosen to be slightly higher than the imaging pixel. For horizontal binning, a standard scientific CCD layout incorporates the summing well, which enables the binned charge to be first stored and read out within a timing chart identical to the un-binned operation mode. With such an implementation, readout noise is theoretically identical for binned and un-binned operations, while additional clock lines are necessary. Because the binning capability does not significantly increase the scientific outcome while it does significantly decrease the mechanical design freedom (such as space, cable stiffness, and thermal isolation), the summing well was not implemented in this sensor.

The next step is to choose the readout port number. The noise is a summation of the quadrature of readout noise and the dark-charge-induced noise. The former consists of the sensor noise and the readout circuit noise. We allocated noise specifications of the on-chip amplifier, the readout circuit, and the dark-charge-induced noise to be  $200$ ,  $200$ , and  $100\ \text{e- rms}$ , respectively. The trade-off of the readout noise and the readout pixel frequency is summarized in Appendix B. In this sensor design case, we chose eight readout ports with a readout rate of  $5.4\ \text{MHz}$ . An example of an un-binned readout scheme is presented in Table II. The output voltage swing of  $4\ \text{V}$  is too large for readout circuitry, and therefore reduced to  $2\ \text{V}$  by the on-chip amplifier with a total gain of  $1/2$ . The responsivity of the readout ports within a sensor differs by a maximum of  $10\%$ . The resulting overall responsivity of the on-chip amplifier ranged from  $0.5$  to  $0.7\ \mu\text{V}/\text{e-}$  among 44 devices. The specification is summarized in Table III.

### III. DETECTOR SYSTEM

#### A. Camera head

The sensor was attached onto an invar package, and wirebonded to an S-shape FPC (flexible printed circuits) cable fitted with a 37 pin micro-D connector. The resulting sensor modules were assembled into camera heads. The micro-D connector was connected to a buffer amplifier described in

TABLE II. Allocated time in the standard un-binned operation sequence for 60 Hz.

Operation	Time for single cycle ( $\mu$ s)	Repetition in a line	Number of cycle in a frame	Time (ms)
Exposure	100	...	1	0.10
Parallel line transfer	3.2 <sup>a</sup>	1	1024 + 6 <sup>b</sup> + 8 <sup>c</sup>	3.32
Serial transfer	0.18 <sup>d</sup>	64 + 4 <sup>e</sup>	1024 + 6 + 8	12.71
Total				16.13

<sup>a</sup>6.4  $\mu$ s is set for 30 Hz operations.<sup>b</sup>The 6 dummy parallel transfer lines are implemented. See Fig. 3 and text.<sup>c</sup>The 8 overscan lines are read for baseline information.<sup>d</sup>0.30  $\mu$ s is set for 30 Hz operation.<sup>e</sup>The 4 dummy serial pixel configuration is implemented. See Fig. 3 and text.

Sec. III B through a glass-hermetic vacuum feedthrough. The sensor module had overhanging geometry in 3 directions, enabling a 4-side buttable assembly with a stepped geometry. An example of the array is presented in Fig. 4. This tiling method minimized the width of the dead pixel region in the array, which became identical to the width of dead region shown in Fig. 3. The stepping level was designed to be 1–1.5 mm. So far we have made three types of detector camera heads, namely, single-, dual-, and octal-sensor detectors (Fig. 5). In the octal-sensor detector case, the sensor array has a central aperture with an opening that can be controlled by a motorized linear feedthrough. In the case of coherent X-ray imaging applications with a 5–7 keV XFEL beam, these camera heads were directly connected to the vacuum chamber.<sup>27</sup> In other applications such as serial femtosecond crystallography, and quantum optics experiments, the camera head chamber was sealed by a beryllium window.

All the single-, dual-, and octal-sensor detectors share a common cooling mechanism. The base surface of the package was bolted onto a cold head, which was cooled by a thermoelectric cooler (TEC) (type: TB-99-1.4-1.05 KRYOTHER, Co.). The hot side of the TEC was cooled by a heat sink with a water channel. The heat dissipation of the sensor was 2 W, which induced a slight temperature gradient over the sensor surface, especially in the overhang region. The maximum temperature difference on the sensor was simulated to be about 0.3 °C from finite element analysis. The sensor could be cooled down to −30 °C using a cooling water temperature of 20 °C. The temperature was monitored by a Pt1000 tem-

perature sensor inside the invar package and stabilized using the PID control of the TEC power, which provided typical stability of  $\pm 0.1$  °C p-p.

## B. Readout board

The readout electronics consisted of a buffer amplifier unit and a readout main board. The buffer amplifier was located in the air side and connected to the sensor through an FPC cable, micro-D connectors and a vacuum feedthrough (Fig. 5(b)). The quasi-differential outputs of the on-chip amplifier were transferred through the tracks in the FPC cable without shielding. This configuration minimized the capacitive load of the on-chip amplifier, and thus reduced the on-chip power dissipation substantially, while rejecting common-mode noise from external noise sources. The vertical and horizontal drivers were implemented onto the main board. The buffer amplifier unit had an active load for the sensor output, an AC coupling to level-shift the signal, and a buffer amplifier. The readout main board featured single-end conversion to subtract real from dummy outputs of the quasi-differential pair of the sensor, a gain amplifier for high- and low-gain video channels, a correlated double sampler, and 16 bit analog-to-digital (ADC) converters (LTC2202, Linear Technology Co.). A simplified schematic for the single read-

TABLE III. Specifications of the MPCCD sensor.

Description	Parameter	Unit
Pixel size	50 × 50	$\mu$ m
Pixel number	1024 × 512	N/A
Imaging area	51.2 × 25.6	mm <sup>2</sup>
Sensing material	Epitaxial silicon	N/A
Sensing layer thickness	50	$\mu$ m
Sensor structure	Front-illumination	N/A
Image format	Full frame transfer	N/A
Operation temperature	0 to −30	°C
Quantum efficiency	80	% at 6 keV
	20	% at 12 keV
Max. frame rate in un-binned mode	60	Hz
Max. pixel readout speed	5.4	MHz
Readout port	8	N/A

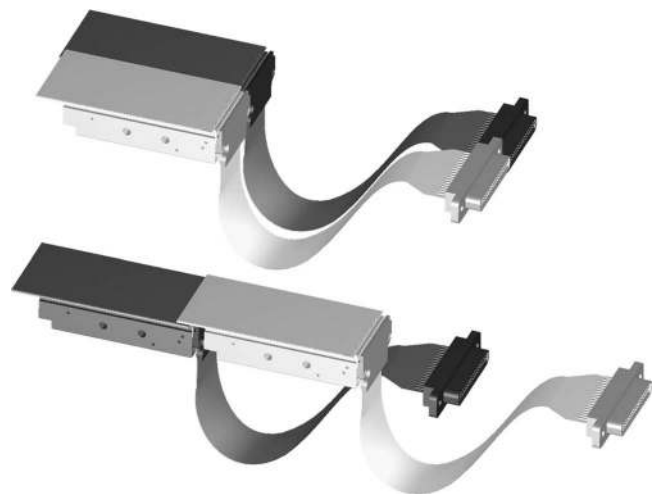


FIG. 4. The package design and tiling modes for the square imaging area (upper) and the rectangular imaging area (lower). The sensors are tiled with steps of 1–1.5 mm to minimize the insensitive area. Their widths for the upper and lower configurations are 300 and 150  $\mu$ m, respectively.



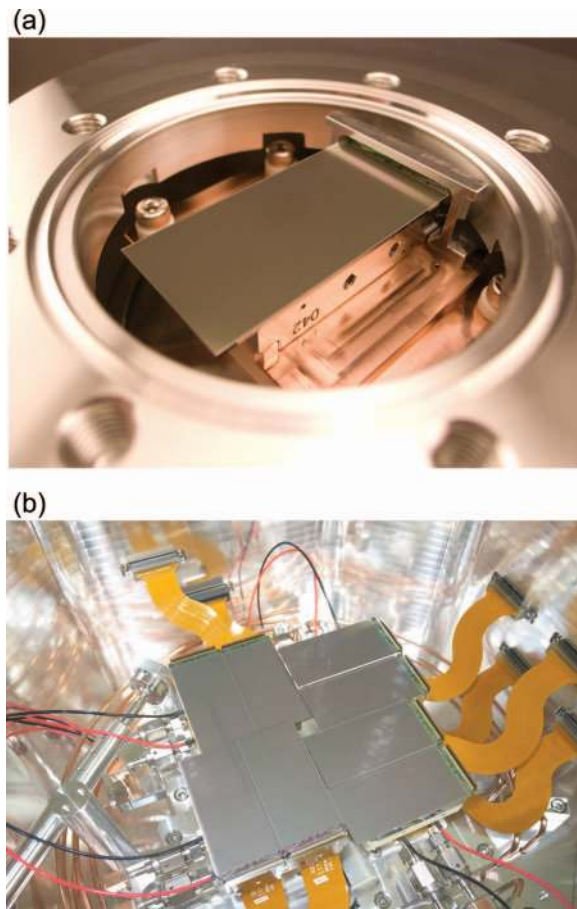


FIG. 5. A Photograph of the single-sensor detector (a) and the octal-sensor detector (b).

out port is shown in Fig. 6. The ADC data were then transferred to an FPGA, and one of the appropriate gain data points was selected and transmitted through the Camera Link base configuration interface. The high-gain channel was designed to have eight times larger gain than the lower one, thus giving effective quantization of 19 bits. In the standard operation

mode, the output data of a pixel had data depth of 16 bits. The lower 15 bits of the output were allocated to the upper 15 bits of one of the high gain or low gain ADC values. The truncated 15 bit data of the high gain channel has been included in digital number (DN) unit in this report. Input referred voltages of the whole readout system are 9.6 and 78  $\mu\text{V}/\text{DN}$  for high and low gain, respectively. Together with the typical sensor responsivity of 0.55  $\mu\text{V}/\text{e}^-$ , 1 DN corresponds to around 17  $\text{e}^-$ , which is smaller than the target system noise of 300  $\text{e}^-$  rms. The fine digitization gave sufficient resolution in the analysis phase, such as the threshold analysis assumed in Appendix A. The most significant bit (MSB) indicated the selected gain. The 16 bit raw-format data were converted to 32 bit floating-point format and calibrated in the data-acquisition system.<sup>28</sup> All the calibration and operation parameters were also transmitted in the header pixel area of the raw-frame data so that each frame data had self-consistency. All the calibration and operation parameters of the detector were stored in the read-only memory of the main board.

All the voltages and clock timing of the drivers were generated by DACs, discrete delay generators, and an FPGA. The parameters of these devices could be set remotely through a Camera Link interface, and used for automated optimization of the CCD performance using dedicated software. Optimization of one sensor to reach the performance reported in this paper typically took 30 min.

#### IV. PERFORMANCE, CALIBRATION, AND DEPLOYMENT

##### A. Radiation hardness

Radiation damage was evaluated using an identical method described in Sec. II A for a fully tested MPCCD sensor. X-ray beams with a size of  $2 \times 7 \text{ mm}^2$  at photon energy of 12 keV were irradiated to 5 areas of the MPCCD sensor at doses of 0.1, 0.33, 1.0, and 2.0 annual dose conditions. Fig. 7 shows the observed temperature dependence, which can be described by the equation of the surface and depletion dark

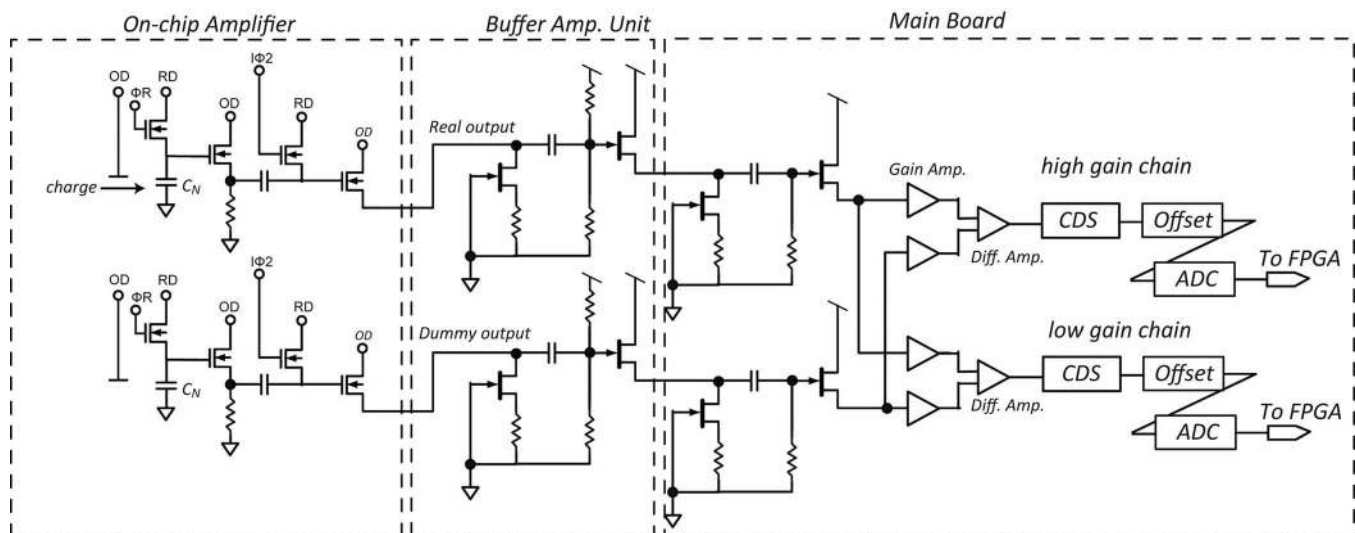


FIG. 6. Overview of the video chain for MPCCD. A schematic for a readout port is shown.



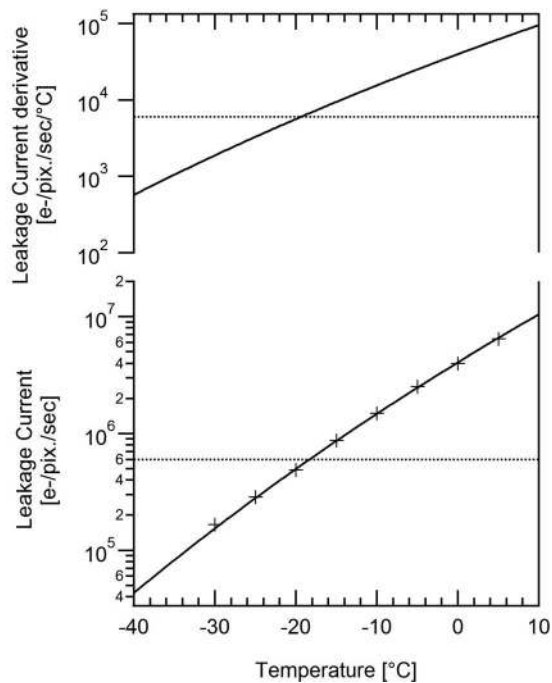


FIG. 7. The dark current measured for a MPCCD sensor after X-ray dose of  $1.6 \times 10^{14}$  photons/mm<sup>2</sup> at a photon energy of 12 keV (one year of the presumed annual X-ray dose). The radiation induces a dark charge 230 times larger than the pre-irradiation condition. The horizontal line at 600 ke-/pixel/s indicates the specification of MPCCD operation to achieve dark induced noise of 100 e- rms.

current, Eq. (1). By cooling the sensor down to  $-20^\circ\text{C}$ , the observed dark current resulting from the radiation dose was well below the target specification of 10 ke-/pixel/frame at 60 frames/s operation, which is equivalent to the allocated dark noise limit of 100 e- rms. The dark current figure of merit,  $D_{FM}$ , as well as the required operation temperature to meet the specification were compared with the COTS devices in Table I. The fabricated device showed less leakage current than the evaluation devices discussed in Sec. II A. The origin of this discrepancy may be due to fabrication lot dependence.

The radiation effect on the flat-band voltage was measured by monitoring the injection diode, which was placed at the top region of the sensor (Fig. 3). The injection threshold variation upon the radiation was measured by sweeping the gate voltage while monitoring the injected charge amount in the MPCCD image through the gated diode. The results indicate the flat-band voltage shifts by about 0.4 V after a single nominal annual dose. The image pixel gate had an optimum voltage range of 1 V, which was smaller than the observed flat-band voltage shift by more than two times. This suggests that the flat-band voltage shift will not cause critical damage on to the CTE up to twice the nominal annual dose. In fact, no CTE degradation was observed in this device after two nominal annual dose.

## B. Noise characteristics

We reduced the frame rate to match the XFEL repetition rate of the SACLA in user operation mode.<sup>47</sup> All the performance reported hereafter was measured at the frame rate of

TABLE IV. Deployed performance of the MPCCD sensor.

Description	Parameters	Unit
System noise	100–250	e- rms
Peak signal <sup>a</sup>	2500–3000	photons/pixel with 6 keV X-ray
	4.1–5.0	Me-/pixel
Radiation hardness	$> 3.2 \times 10^{14}$	photons/mm <sup>2</sup> with 12 keV X-ray
Frame rate	30	Hz
Pixel readout speed	3.3	MHz
Dark signal	600	ke-/pixel/s at $20^\circ\text{C}$

<sup>a</sup>CTE limited Full well capacity. Performance is dependent on device lot and injection signal pattern.

30 Hz. The associated timing sequence is listed in Table II. Table IV summarized the observed performance.

The noise characteristics such as pixel-to-pixel variation in a single frame, and frame-to-frame deviation are critical for single photon detection. The raw image had an apparent stripe pattern as shown in Fig. 8(a). A horizontal profile averaged over 64 rows had a stepped structure with 70 DN p-p (1200 e- p-p) as shown in Fig. 8(c). This was identified to result from the offset variation of the readout ports, which were not calibrated enough by the analog offset adjustments (see Sec. III B and Fig. 6). A smaller slope was observed for each readout port with less than 5 DN (90 e-) due to the ramping of the serial readout circuit during the reading sequence. From the vertically perspective, a slope-like feature less than 20 DN (350 e-) exists at the top of the image due to the slow circuit fluctuation (Fig. 8(a)). Line profile averaged over 64 columns of the port 1 is shown in Fig. 8(d). These profiles are stable over time enough that any non-uniformity can be eliminated by subtracting the average background image down to 4 DN rms (70 e- rms), well below the readout noise level (Figs. 8(c) and 8(d)). By using this background-calibrated data, the system gain was evaluated by a Fe<sup>55</sup> source. A typical Fe<sup>55</sup> histogram is shown in Fig. 11. It indicates that the single photon signal can be distinguished from the background noise by an appropriate threshold. Readout noise for 44 sensors was measured at the sensor temperature of  $-20^\circ\text{C}$  at a readout rate of 3.3 MHz, and was determined to be 100–250 e- rms.

The mean of all the pixel values in a frame, defined as frame offset in this report, varied in hour time scale (Fig. 9) due to temperature variation and low frequency noise. It is possible to compensate for these inconsistencies by subtracting the data in the over-scan-region (OSR) pixels. The frame offset after this calibration is shown in Fig. 9. The OSR calibration yielded frame offset fluctuation over 10 h to be less than 2.5 DNp-p (45 e-p-p).

## C. Linearity and full well capacity

Linearity was evaluated by illuminating an X-ray beam generated by Cu target source (micro-focus X-ray source L9631, Hamamatsu Photonics). The digital output of the high gain and low gain video chains were measured by changing the exposure time in an operation mode dedicated for calibration, where both the high- and low-gain raw data were

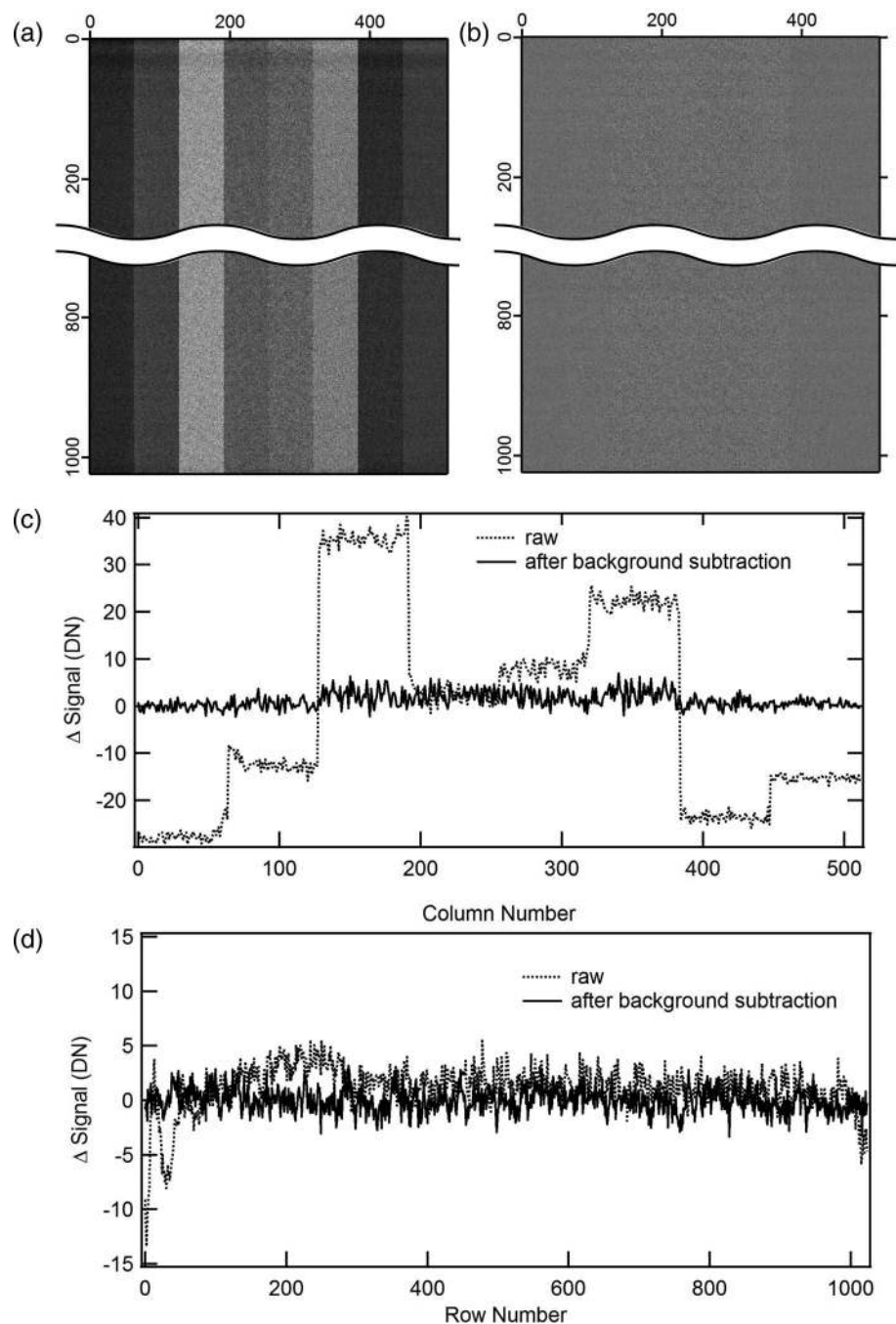


FIG. 8. Dark images of raw data (a) and background subtracted data (b). The line profiles averaged over 64 lines for the horizontal (c) and vertical (d) directions are shown for quantitative clarification of the background character.

transmitted through the Camera Link interface. The obtained results are shown in Fig. 10. The digital output of the high gain channel saturated around 600 ke $^{-}$  (Fig. 10(a)). In the standard readout mode, output data were switched pixelwise to the low gain channel if the high gain value exceeded a threshold around 500 ke $^{-}$ . The calibration procedure described later in Sec. IV D yielded signal intensity with good linearity as shown in Fig. 10(b). The linear fitting gave residual measures less than 30 ke $^{-}$ . In this device case, the residual was sharply increased around 4.5 Me $^{-}$ , which was the CTE-limited full well. The CTE-limited full well ranged from 4.1 to 5.0 Me $^{-}$ , depending to the device lot and the optical illumination pat-

terns. In the small signal case, the ratio of residual to the signal intensity (residual ratio) was deemed more important than the absolute magnitude of the residual and was less 1% (Fig. 10(d)). This corresponds to the requirement that the systematic error of the signal be less than 1% of the signal. Fitting to a cubic-spline function can yield a better residual ratio, as low as 0.3% (Fig. 10(d)).

Linearity of the CCD is determined by the (1) charge generation, (2) charge transfer, (3) charge-to-voltage conversion, and (4) voltage-to-digital conversion steps. All the detection steps after the charge generation are identical for X-ray and optical light illumination cases. If we can use the optical light

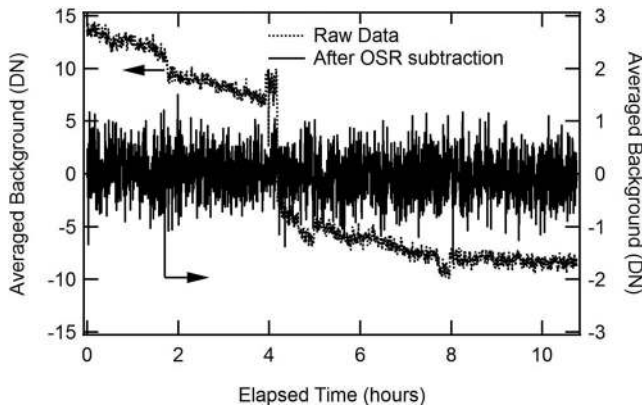


FIG. 9. The time dependence of the mean of all the pixels in the port in dark condition (port offset) is shown. The port offset after subtracting the 24 lines in the over-scan region (OSR) is shown for comparison.

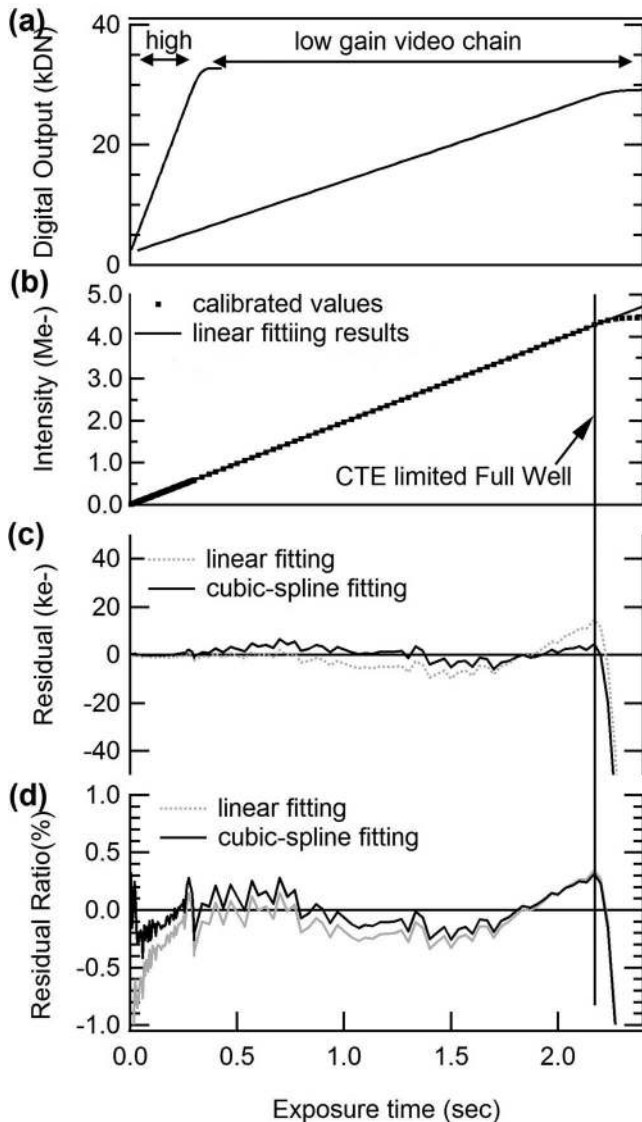


FIG. 10. The signal intensity dependence on the exposure time under constant X-ray illumination in digital output (a) and calibrated intensity (b). The linear fitting to the calibrated data is also shown. Calibrations with the linear and cubic-spline fittings were carried out. The resulting residual and ratio of the residual to the calibrated intensity defined as residual ratio are indicated in (c) and (d), respectively.

for device testing, we can simplify many of the testing procedures. Now let us look at the charge generation step. The linearity against X-rays may differ from the optical light if the pixel has significant trap sites inside the pixel; traps of MOS CCDs are generally located at the interface between epitaxial silicon and gate oxide, and the difference of the attenuation depth between X-ray and the optical light may make the trapping probability different. Measured charge amount becomes smaller by the absorbed charge by the traps. This gives the nonlinearity, or more precisely an additional offset. In general CCDs, however, the traps are less than 10 electrons and does not create substantial difference in both the illumination cases. In fact, the parallel CTE of the present CCD was over 99.995% with 10 ke- signal indicating that each pixel had traps less than 5 electrons per pixel. We have recorded the data by replacing the X-ray to an optical illumination by using a light-emitting diode (LED) with a wavelength of 630 nm. The resulting fitting parameters were identical within the experimental error. We therefore concluded that linearity can be assessed by the optical method. In the routine calibration procedure described in Sec. IV D, we used the LED instead of X-rays.

#### D. Calibration

Calibration of each sensor-electronics pair was performed once after the assembly. The procedure consisted of three categories, static, dynamic, and leakage calibrations. The static procedure calibrated the static amplifier behavior of each readout port described in Sec. II C by recording the LED with a wavelength of 630 nm. This procedure gave parameters on the analog offset  $B_{static}$  and gain  $G$  in all the high- and low-gain video chains at the operation temperature (16 chains in total). Then,  $Fe^{55}$  source signal was measured to obtain the output digital number per unit electron signal, or the responsivity  $R$  (Fig. 11, Sec. III B). The responsivity was used to calibrate inter-sensor gain difference. In summary, the static calibration can be expressed as

$$I_{static}(i, j, s, n) = R(s)G(p, g)\{I_R(i, j, s, n, g) - B_{static}(p, g)\}, \quad (3)$$

where  $I_R$  denotes the raw digital number with row number  $i$ , the column number  $j$  of sensor id  $s$ , the frame number  $n$ , and the appropriate gain of the video channels  $g$ . The port number is indicated as  $p$ . In this static calibration, the background was calibrated by each video chain but not pixelwise.

In the next step, dynamic calibrations on the inter-port crosstalk and background drift during the experimental runs were carried out. We observed that the inter-port crosstalk was linearly dependent to the other port intensity. The magnitude was typically less than 100 ppm with some pairs having 1000–2000 ppm. The background drift was compensated for using the average of overscan pixel levels  $B_{dynamic}(p, n)$ . In the last step, pixel dependent leakage current is subtracted by recording an average of the dark frames,  $B_{leak}(i, j)$ , typically after



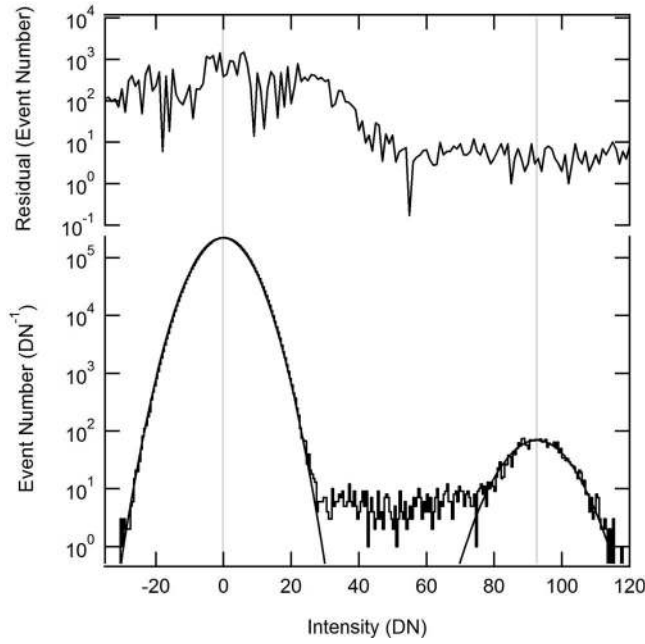


FIG. 11. An example of a signal intensity histogram under the illumination of  $\text{Fe}^{55}$  source (5.9 keV). The fitted line with two Gaussian functions is also shown in the lower panel with residual distribution. The readout noise was 103 e- rms.

the acquisition of an experimental run:

$$I_{\text{dynamic}}(i, j, n, s) = f_{\text{crosstalk}}(I_{\text{static}}(i, j, n, s), I_{\text{static}}(i', j', n, s), \times I_{\text{static}}(i'', j'', n, s) \dots) - B_{\text{dynamic}}(p, n), \quad (4)$$

$$I_{\text{calibrated}}(i, j, n, s) = I_{\text{dynamic}}(i, j, n, s) - B_{\text{leak}}(i, j), \quad (5)$$

where  $f_{\text{crosstalk}}$  denotes the calibration function for the crosstalk, and is a function of the intensity of the other seven pixels which are simultaneously read out. All these calibration parameters except for  $B_{\text{dynamic}}(p, n)$  were saved into the read-only-memory (ROM) of the readout electronics and were transmitted as header data onto the image raw data.  $B_{\text{dynamic}}(p, n)$  was calculated inside the FPGA of the readout board on-the-fly, and transmitted as header data as well. Calibration calculations of Eqs. (3) and (4) were carried out at the SACLA data-acquisition system (DAQ) by using these header files. All the parameters were measured with sufficient pixel numbers so that the parameter errors did not contribute to the system noise.

The meta-data of each frame contain all the information on the calibration parameters and the operating condition except for the dark frame data  $B_{\text{leak}}(i, j)$ . From the user point of view, this *quasi-self-consistent* data structure at the frame level simplifies the analysis scheme and DAQ design at the cost of the meta-data size. The data size in our implementation is 1 kbyte, which is small compared to the binary frame data size of about 1 Mbyte.

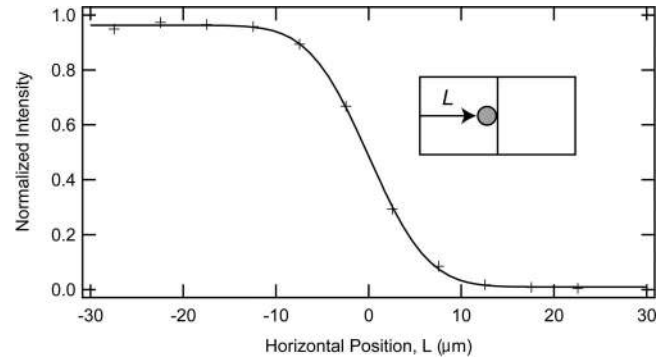


FIG. 12. The dependence of the signal intensity of a pixel on the X-ray beam position with respect to the pixel's center. Signal intensity is normalized by the total intensity of its surrounding 81 pixels. The data are applied with the fitting to an error function. The deconvoluted PSF has standard deviation of  $3.6 \mu\text{m}$ .

### E. Point spread function

In order to evaluate PSF in the high injection regime, X-ray laser pulses provided by SACLA were injected to a MPCCD sensor at a photon energy of 10 keV at BL3.<sup>29</sup> The sensor was cooled to  $-20^\circ\text{C}$ . In front of the MPCCD sensor, the X-ray laser pulses were attenuated by using a Si single crystal and then shaped by a pinhole. The pinhole was made of a tungsten plate with a thickness of  $20 \mu\text{m}$  and a diameter of  $10 \mu\text{m}$ . The pinhole was placed 200 mm upstream of the sensor. Under these conditions, the Fraunhofer diffraction could be neglected. The number of injected charges was 2.74 Me-,

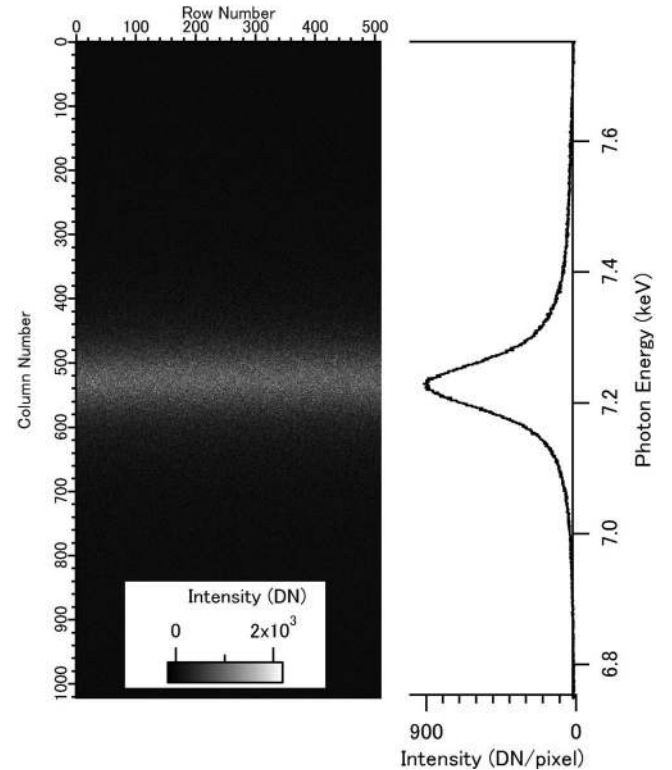


FIG. 13. The MPCCD image recorded by an in-line spectrometer at SACLA Beamline 3 (left). The Bragg diffraction pattern of a diamond (111) is detected. The image is processed to yield the spectrum shot-by-shot (right) and is later used in most of the experiments as diagnostic data.



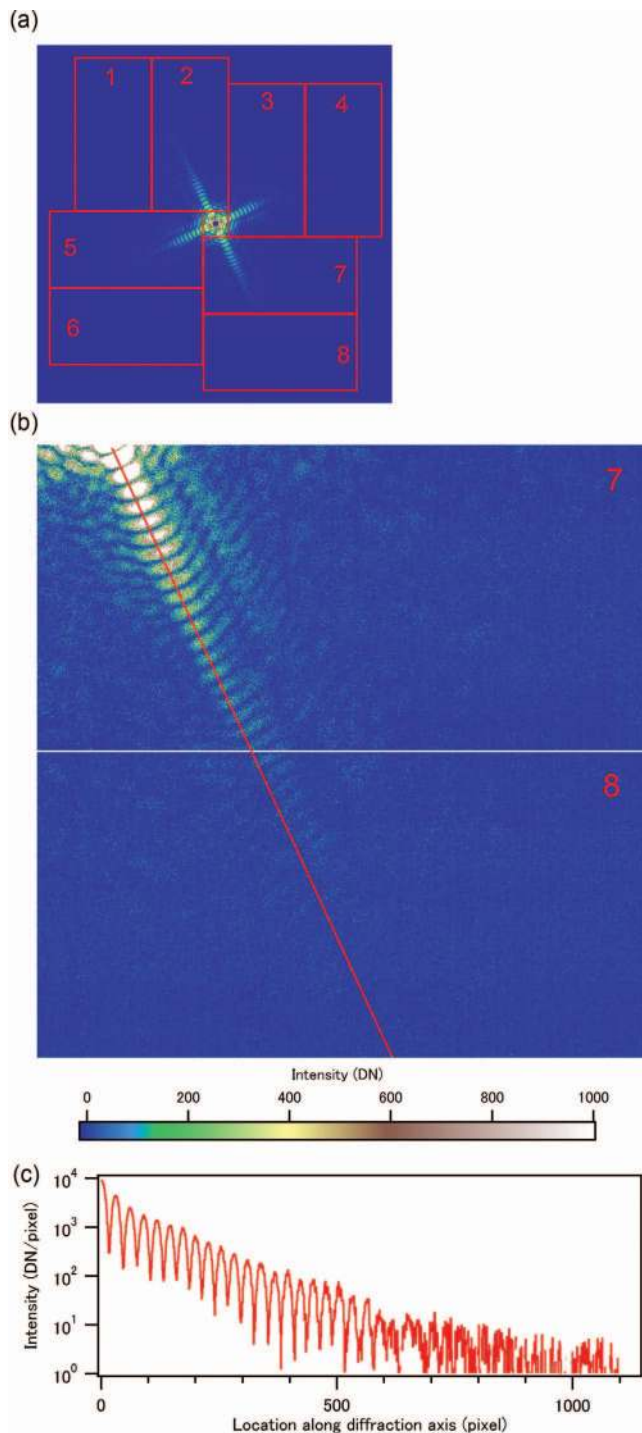


FIG. 14. The MPCCD data recorded in the coherent diffraction experiments. Data are taken by upstream octal-sensor detector and downstream dual-sensor detector.<sup>27</sup> The calibrated data of the two detectors is shown (a). Two sensors located in the down-right segment of the octal-sensor detector are shown to depict the details of the data (b). Along the strong speckle pattern line labelled as a red line in (b), line profile with 50 pixel width is shown in (c).

corresponding to 1000 photons. The irradiation areas were scanned from one pixel center to the next pixel center at a step of  $5 \mu\text{m}$ . The results are presented in Fig. 12. The plots are data averaged with 60 frames. The signal ratio is defined by the signal of the pixel of interest normalized by the summation of signal intensity of the surrounding pixels (a  $9 \times 9$  matrix with 81 pixels in total).

The charge spread was evaluated by recording image data upon moving the sensor in a horizontal direction. The signal of the pixel was plotted against the pixel position, as shown in Fig. 12. The PSF was assumed to have a Gaussian profile and the width was obtained by fitting an error function. The deconvoluted PSF from the pinhole circle had a Gaussian profile with a standard deviation of  $3.3 \pm 0.3 \mu\text{m}$  in good agreement with the simulated value of  $4.6 \mu\text{m}$  at 5.0 MeV injection described in Sec. II B.

## F. Deployment example

The MPCCD single-sensor detector was first used in the commissioning phase of the SACLA facility. The spontaneous X-ray emission from the undulators was used for the accurate alignment of the electron beam trajectory and the undulators.<sup>30</sup>

SACLA BL3 has an in-line spectrometer that records photon energy with moderate resolution.<sup>29</sup> The equipment consists of a speckle-free nanocrystal diamond foil and a MPCCD single-sensor detector that records X-ray Bragg diffraction. An example image is shown in Fig. 13. The Bragg diffraction pattern of a diamond (111) was successfully detected shot-by-shot. The image was processed through the SACLA DAQ system to yield and save every spectrum. This in-line monitor is operating since the first user<sup>31,32</sup> beamtime of March 2012 24 h a day. The results have been used in most experiments as XFEL diagnostic data.

Another example is a tandem usage of an octal-sensor detector and a dual-sensor detector in the coherent X-ray diffraction imaging experiments. Details of the apparatus are described in Ref. 27. Fig. 14(a) shows the diffraction pattern of the cube-shaped copper particle<sup>33</sup> after merging the two MPCCD detectors. Details of the two sensors (#7 and #8) located in the upstream octal-sensor detector is shown in Fig. 14(b). The data were calibrated by the method described in Sec. IV D. Clear speckle pattern was successfully obtained. The line profile with a width of 50 pixels is shown in Fig. 14(c). The pattern with an average intensity ranging from 10 000 to 1 DN/pixel (230 ke- to 23 e-) was clearly observed. Similar setting was also used and reported in Ref. 34.

After one and a half years of operations, 85% of user experiments utilized MPCCD detectors as the main data collection apparatus. Some of the results were published in Refs. 31, 32, and 35–41.

## V. CONCLUSION AND OUTLOOK

In this report, we have presented developments of the MPCCD detector for our XFEL facility, SACLA. We successfully demonstrated X-ray radiation hardness against two presumed annual fluence of  $3.2 \times 10^{14}$  photons/ $\text{mm}^2$  at 12 keV photon energy, which corresponds to 1.16 MGy. Damaging effects to the flat-band voltage shift and an increase of the dark current were identified. The former was determined to be 0.4 V per nominal annual dose, which is smaller than the operation window of 1 V, which indicates that CTE degradation can be avoided by applying an appropriate voltage adjustment

to the image gate clocks. The latter can be compensated by cooling the sensor; after one presumed annual fluence of  $1.6 \times 10^{14}$  photons/mm<sup>2</sup> at 12 keV, a temperature of  $-17^\circ\text{C}$  was required to maintain the noise induced by the dark charge to less than 100 e- rms. A camera head with a simple TEC cooler was fabricated. It was able to cool the sensor down to  $-30^\circ\text{C}$ , which could prevent apparent degradation to the sensor from the two presumed annual X-ray dose.

A detector system with large number of readout ports makes the readout rate lower, and the readout noise lower. However such system increases the complexity by a higher cost in calibration, a greater on-chip power dissipation and an increase of the number of electrical lines inducing less thermal isolation between the sensor and the readout electronics. The latter two result in less freedom in mechanical design of the camera head. The trade-offs are also discussed in terms of the noise equivalent signal, dynamic range, and readout pixel frequency in Appendix B. The identical design approach is applicable to a MOS CCD device with thicker depletion as explored for other optical missions.<sup>42</sup> We are currently targeting a depletion depth of 280  $\mu\text{m}$ .

Response of the sensor to intense femtosecond X-ray pulses is a common concern for X-ray pixel detectors for XFEL applications. One of the important effects is the PSF degradation by high injection of the signal charge. We addressed this phenomenon by device simulations and experiments, and were able to demonstrate that the developed MPCCD sensors had only a slight degradation of PSF to a standard deviation of  $3.3 \pm 0.3 \mu\text{m}$  with 2.74 Me- injection, which is small enough for a pixel size of 50  $\mu\text{m}$ . The experimental results also indicate that the two-phase pixel design selected in this work was able to keep the internal electric field high enough to collect the signal charge against the induced current to the image gate lines.

These results together with recent deployment examples show that optimally designed multi-port CCD device is one of the most powerful X-ray 2D detector options for XFEL experiments.

## ACKNOWLEDGMENTS

The authors appreciate the many valuable discussion with Yoshinori Nishino and Tetsuya Ishikawa and support from the engineering division, especially Kunihiro Fujiwara and Manabu Kimoto. This work is partly supported by a grant for XFEL key technology to T.H. The authors also appreciate e2v Ltd. XCam Ltd. and Meisei Electric Co. Ltd. for providing of the CCD sensors for the radiation hardness evaluation, building cameras for these sample devices, and manufacturing the readout electronics, respectively. The authors acknowledge the provision of the raw data of Fig. 14 by Yuki Sekiguchi, Tomotaka Oroguchi, and Masayoshi Nakasako of Department of Physics, Keio University.

## APPENDIX A: READOUT NOISE AND SINGLE PHOTON DETECTION

Single photon detection can be achieved if the signal charge is significantly larger than the readout noise. The sig-

nal charge of the X-ray photon absorbed around the edge or corner of the pixel is shared and the charge amount in each pixel decreases. Single photon detection for these events demands lower readout noise. A general trade-off of the charge spread, readout noise, and the detection accuracy should be reviewed in order to deduce the readout noise specification. The relationship is also important in the analysis of the data. Due to such demands, elaborate software development was required to simulate the detector response.<sup>23</sup> In this appendix, the simplified figure of merit is discussed in order to derive the general trade-off relationship.

The detection capability is characterized here by two parameters, namely, false signal probability *FSP* and un-detection probability, *UDP*. The former is defined as the ratio of the pixel data that exceeds the threshold value  $z_t$ . In the case of Gaussian distribution noise, it can be described by

$$FSP(z) = 1 - CDF_{\text{gauss}}(z) = \frac{1}{2} \left( 1 - \text{Erf} \left( \frac{z}{\sqrt{2}} \right) \right), \quad (\text{A1})$$

where  $CDF_{\text{gauss}}(z)$  denotes the cumulative distribution function of the readout noise.

In order to derive the simple figure-of-merit function for un-detection probability, *UDP*, we consider the single photon to be detected if the signal charge of the pixel where the photon is absorbed exceeds the threshold value,  $z$ , used in the data analysis. In this appendix, pixel shape is assumed to be square and the length scale is normalized to the pixel size. In addition, all the photoabsorption events are assumed to have an identical charge spread with Gaussian distribution function,  $g$ , with standard deviation of  $\sigma_{\text{nor}}$  independent on the depth where X-ray photon is absorbed. Then, signal charge within a pixel  $ij$ ,  $C_{ij}$ , can be described by

$$C_{ij}(x_c, y_c) = \int_{(x,y) \in S_{ij}} g(x, y, x_c, y_c, \sigma_{\text{nor}}) dx dy, \quad (\text{A2})$$

where  $x_c$  and  $y_c$  represent the position of X-ray absorption in the image surface plane  $xy$ . Here the integral is only within the pixel region  $S_{ij}$  of the pixel  $ij$ . The un-detection probability, *UDP*, can then be expressed by the cumulative density function, *CDF* of the convolution of the probability density function  $PDF_{C_{ij}, S_x}$  of  $C_{ij}$ , and noise distribution  $g$  as follows:

$$UDP = CDF_{C_{ij}, S_x, n}(z) = \int_{-\infty}^z PDF_{C_{ij}, S_x} \otimes g(n). \quad (\text{A3})$$

The *UDP* in the case of MPCCD with 300 e- rms noise, and X-ray photon energy of 6 keV, and 12 keV is shown in Fig. 15 as a function of threshold value,  $z$ , and  $\sigma_{\text{nor}}$ . The signal charge and the length units are normalized to the charge amount created by a single photon, and the pixel size. At a photon energy of 6 keV with 300 e- rms readout noise with  $z = 0.45$ , the *UDP* becomes 0.15 and 0.064 for un-binned and  $2 \times 2$  binned operation, respectively. The *UDP* is decreased for 12 keV to 0.10 and 0.034 for un-binned and  $2 \times 2$  binned operations. Here photon absorption probability, or quantum efficiency, is not included. The associated decrease of the detection probability should be taken into account in real device cases.

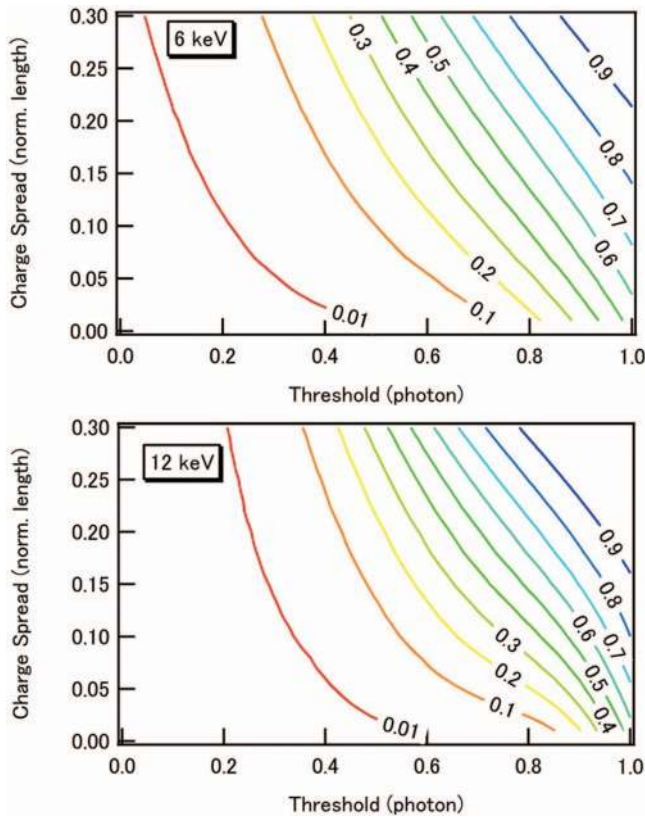


FIG. 15. Un-detection Probability as a function of the standard deviation of a Gaussian-shape charge spread and the threshold. Two cases with the readout noise of 0.182 (upper) and 0.0912 photon (lower) are shown. These corresponds to 6 keV and 12 keV X-ray photon cases with 300 e- rms noise, respectively.

## APPENDIX B: TRADEOFFS BETWEEN READOUT SPEED, NOISE, AND DYNAMIC RANGE

Operations of XFEL facilities using normal conducting accelerator cavities under construction and designed phases generally have rates from 60 to a few hundreds pulses per second. Therefore it is of interest to investigate the trade-offs on the frame rate in this multi-port CCD design. Generally, faster readout rates lead to higher readout noise floors. The quantitative trade-offs among the readout speed, noise, and the ratio between them, *or the dynamic range*, are summarized in this appendix.

In the higher frame rate with multiple readout ports, the parallel transfer frequency,  $f_p$ , contributes significantly to the frame rate  $f_{frame}$ . The frame rate can be described as follows for an image format with  $X$  and  $Y$  readout pixels in the parallel and serial directions, respectively:

$$1/f_{frame} = (1/f_p) \cdot X + (1/f_s) \cdot X \cdot Y/N_{port},$$

where  $f_p$  and  $f_s$  are parallel and serial readout frequencies, respectively. Generally, parallel transfer frequency is slower than serial transfer (i.e.,  $f_p < f_s$ ). The highest frame rate is then achieved with a full column parallel readout scheme where  $Y = N_{port}$ . However, this scheme generally demands a dedicated integrated circuit, becoming more power hungry. In the design reported in this paper, a target noise equivalent signal ( $NES$ ) of 300 e- rms for 60 frames/s operation is achieved with

$f_p = 0.31$  MHz and  $f_s = 5.4$  MHz with readout pixels of  $X = 544$  and  $Y = 1038$  with  $N_{port} = 8$  (Tables II and III).

Next, we look into the trade-offs with regard to the on-chip amplifier. In the course of the CCD sensor design, the readout noise, peak signal, and the ratio between them *or dynamic range*, are of critical importance in the optimization of the sensor. The trade-offs among these parameters are dependent on manufacturing processes. In the design with the floating node capacitance matched to the input transistor gate-source capacitance, the input-referred readout noise can be minimized. This optimum design gives us the following relation as a function of the serial readout rate of  $f_s$ :

$$NES = \frac{\sqrt{2C_N(A_1 + A_2 f_s/f_c)}}{e}, \quad (B1)$$

where  $NES$ ,  $C_N$ ,  $f_c$ , and  $e$  are  $NES$  in the rms. electrons unit, the input node capacitance, the corner frequency of the input transistor of the first stage amplifier, and the elementary charge, respectively.<sup>43,44</sup> Here the cut-off frequency of the video chain is assumed to be  $2f_s$ . Note that the factor 2 in the square root of the equation is introduced by the quasi-differential output implemented in the current design. If the external noise source is well isolated from the sensor electronics, this can be omitted in the implementation, and  $NES$  improves better by a factor of  $\sqrt{2}$ .

The factors,  $A_1$  and  $A_2$ , are process parameters. These are dependent on the manufacturing process. In the optimum design with gate matching condition, these parameters become independent from the transistor size. In the process employed for the current MPCCD,  $f_c$  is 150 kHz. The input node capacitance for the present sensor is designed to  $C_N = 200$  fF with a voltage swing  $V_{sw} = 4$  V. Under the operation modes with  $f_p = 3.3$  MHz and 5.4 MHz,  $NES$  is estimated to be 94 and 120 e- rms, respectively. The former value accords well with the readout noise of the detector recorded to be 103 e- rms (Fig. 11).

Now we discuss the extension of this output circuit to other readout frequencies. The peak signal,  $Q_{max}$ , is set by  $V_{sw}$  and the input node capacitance,  $C_N$  as

$$Q_{max} = V_{sw} \cdot C_N. \quad (B2)$$

The dynamic range,  $DR$ , is defined as

$$DR = Q_{max}/NES. \quad (B3)$$

Hence, the optimum design gives the trade-off relation of  $NES$  as

$$NES = \frac{2DR(A_1 + A_2 f_s/f_c)}{e^2 V_{sw}}. \quad (B4)$$

Therefore, we see that  $f_s$  can be increased either by increasing  $NES$ , or by decreasing the target  $DR$ . See Table II for the time allocation of the present device for 60 frames/s operations. Compared with other fast scientific CCDs for XFEL applications using intensive column parallel readout,<sup>45,46</sup> the MPCCD described in this paper has a higher  $f_s$  by accepting a higher  $NES$ , while maximizing  $DR$ . In addition, the resulting fewer readout ports simplifies the camera circuitry. For the higher frame rate of 120 Hz, which is the repetition rate of the LCLS facility,<sup>1</sup> there are four options; using  $2 \times 2$  analog



binning operations with the current device, reducing X to half ( $512 \times 512$  pixels), increasing the port number to about 24, or designing the amplifier with a peak signal half the value of the present device.

- <sup>1</sup>P. Emma *et al.*, *Nat. Photonics* **4**(9), 641–647 (2010).
- <sup>2</sup>T. Ishikawa *et al.*, *Nat. Photonics* **6**(8), 540–544 (2012).
- <sup>3</sup>H. T. Philipp *et al.*, *Nucl. Instrum. Methods Phys. Res., Sec. A* **649**(1), 67–69 (2011).
- <sup>4</sup>B. Henrich *et al.*, *Nucl. Instrum. Methods Phys. Res., Sec. A* **633**, S11–S14 (2011).
- <sup>5</sup>M. Porro *et al.*, *Nucl. Instrum. Methods Phys. Res., Sec. A* **624**(2), 509–519 (2010).
- <sup>6</sup>A. Blue *et al.*, *Nucl. Instrum. Methods Phys. Res., Sec. A* **607**(1), 55–56 (2009).
- <sup>7</sup>G. A. Carini *et al.*, *Nucl. Instrum. Methods Phys. Res., Sec. A* **649**(1), 75–77 (2011).
- <sup>8</sup>S. Tsuneta *et al.*, *Sol. Phys.* **136**(1), 37–67 (1991).
- <sup>9</sup>B. E. Burke *et al.*, *IEEE Trans. Nucl. Sci.* **41**(1), 375–385 (1994).
- <sup>10</sup>Y. Tanaka *et al.*, *Publ. Astron. Soc. Jpn.* **46**(3), L37 (1994).
- <sup>11</sup>B. E. Burke *et al.*, *IEEE Trans. Electron Devices* **44**(10), 1633–1642 (1997).
- <sup>12</sup>L. Struder *et al.*, *Astron. Astrophys.* **365**(1), L18–L26 (2001).
- <sup>13</sup>M. J. L. Turner *et al.*, *Astron. Astrophys.* **365**(1), L27–L35 (2001).
- <sup>14</sup>K. Koyama *et al.*, *Publ. Astron. Soc. Jpn.* **59**, S23–S33 (2007).
- <sup>15</sup>S. M. Gruner *et al.*, *Rev. Sci. Instrum.* **73**(8), 2815–2842 (2002).
- <sup>16</sup>J. R. Janesick, *Scientific Charge-Coupled Devices* (SPIE Press, Bellingham, WA, 2001).
- <sup>17</sup>G. W. Fraser *et al.*, *Nucl. Instrum. Methods Phys. Res., Sec. A* **350**(1–2), 368–378 (1994).
- <sup>18</sup>A. Owens *et al.*, *Nucl. Instrum. Methods Phys. Res., Sec. A* **491**(3), 437–443 (2002).
- <sup>19</sup>G. F. Moroni *et al.*, *Exp. Astron.* **34**(1), 43–64 (2012).
- <sup>20</sup>J. H. Hubbell *et al.*, *J. Phys. Chem. Ref. Data* **4**(3), 471–538 (1975).
- <sup>21</sup>T. P. Ma and P. V. Dressendorfer, *Ionizing Radiation Effects in MOS Devices and Circuits* (Wiley, New York, 1989).
- <sup>22</sup>K. Tamasaku *et al.*, *Nucl. Instrum. Methods Phys. Res., Sec. A* **467–468**, 686–689 (2001).
- <sup>23</sup>G. Potdevin *et al.*, *JINST* **4**, P09010 (2009).
- <sup>24</sup>S. M. Sze and K. K. Ng, *Physics of Semiconductor Devices*, 3rd ed. (Wiley-Interscience, Hoboken, NJ, 2007).
- <sup>25</sup>D. B. M. Klaassen, *Solid-State Electron.* **35**(7), 953–959 (1992).
- <sup>26</sup>Y. Ishihara *et al.*, *ISSCC Dig. Tech. Pap.* **25**, 168 (1982).
- <sup>27</sup>M. Nakasako *et al.*, *Rev. Sci. Instrum.* **84**(9), 093705 (2013).
- <sup>28</sup>M. Yamaga *et al.*, *Proceedings of ICALPCS*, Art. number TUCAUST06, 2011.
- <sup>29</sup>K. Tono *et al.*, *New J. Phys.* **15**, 083035 (2013).
- <sup>30</sup>T. Tanaka *et al.*, *Phys. Rev. ST Accel. Beams* **15**(11), 110701 (2012).
- <sup>31</sup>T. Katayama *et al.*, *Appl. Phys. Lett.* **103**(13), 131105 (2013).
- <sup>32</sup>Y. Obara *et al.*, *Opt. Express* **22**(1), 1105–1113 (2014).
- <sup>33</sup>C. H. Kuo *et al.*, *Adv. Funct. Mater.* **17**(18), 3773–3780 (2007).
- <sup>34</sup>C. Song *et al.*, *J. Appl. Crystallogr.* **47**(1), 188–197 (2014).
- <sup>35</sup>Y. Inubushi *et al.*, *Phys. Rev. Lett.* **109**(14), 144801 (2012).
- <sup>36</sup>K. Tamasaku *et al.*, “X-ray two-photon absorption competing against single and sequential multiphoton processes,” *Nat. Photonics* (published online).
- <sup>37</sup>T. Kimura *et al.*, *Nat. Commun.* **5**, 3052 (2014).
- <sup>38</sup>Y. Takahashi *et al.*, *Nano Lett.* **13**(12), 6028 (2013).
- <sup>39</sup>T. Hara *et al.*, *Phys. Rev. ST Accel. Beams* **16**(8), 080701 (2013).
- <sup>40</sup>K. Tamasaku *et al.*, *Phys. Rev. Lett.* **111**(4), 043001 (2013).
- <sup>41</sup>T. Hara *et al.*, *Nat. Commun.* **4**, 2919 (2013).
- <sup>42</sup>D. E. Groom *et al.*, *Nucl. Instrum. Methods Phys. Res., Sec. A* **442**(1–3), 216–222 (2000).
- <sup>43</sup>M. S. Robbins, in *Single-Photon Imaging*, edited by P. Seitz and A. J. P. Theuwissen (Springer, 2011), Chap. 6, pp. 103–122.
- <sup>44</sup>D. J. Burt, *GEC Journal of Research* **12**(3), 130–140 (1995).
- <sup>45</sup>L. Struder *et al.*, *Nucl. Instrum. Methods Phys. Res., Sec. A* **614**(3), 483–496 (2010).
- <sup>46</sup>P. Denes *et al.*, *Rev. Sci. Instrum.* **80**, 083302 (2009).
- <sup>47</sup>The pulse frequency of the SACLA facility was designed to be 60 Hz, but started the user operation with 10 Hz and increased the frequency to 30 Hz. In order to optimize the detector performance under this condition, we reduced the frame rate to 30 Hz to achieve better noise performance (Appendix B).